

OPEN ACCESS

Evaluating Long-Term Cycling Degradation in Cylindrical Li-Ion Batteries Using X-ray Tomography and Virtual Unrolling

To cite this article: Anmol Jnawali *et al* 2023 *J. Electrochem. Soc.* **170** 090540

View the [article online](#) for updates and enhancements.

You may also like

- [Erratum: "The GRIFFIN Project—Formation of Star Clusters with Individual Massive Stars in a Simulated Dwarf Galaxy Starburst" \(2020, ApJ, 891, 2\)](#)
Natalia Lahén, Thorsten Naab, Peter H. Johansson et al.
- [Erratum: "Simple Physics and Integrators Accurately Reproduce Mercury Instability Statistics" \(2023, ApJ, 944, 190\)](#)
Dorian S. Abbot, David M. Hernandez, Sam Hadden et al.
- [Signature of Supersonic Turbulence in Galaxy Clusters Revealed by AGN-driven H Filaments](#)
Haojie Hu, , Yu Qiu et al.



245th ECS Meeting • May 26-30, 2024 • San Francisco, CA

Don't miss your chance to present!

Connect with the leading electrochemical and solid-state science network!

Deadline Extended: December 15, 2023

[Submit now!](#)





Evaluating Long-Term Cycling Degradation in Cylindrical Li-Ion Batteries Using X-ray Tomography and Virtual Unrolling

Anmol Jnawali,¹ Matt D. R. Kok,^{1,2} Muthu Krishna,³ Mina Abedi Varnosfaderani,³ Daniel J. L. Brett,^{1,2} and Paul R. Shearing^{1,2,4,z} 

¹Electrochemical Innovation Lab, Department of Chemical Engineering, UCL, London WC1E 7JE, United Kingdom

²The Faraday Institution, Quad One, Harwell Science and Innovation Campus, Didcot OX11 0RA, United Kingdom

³Advanced Cell Engineering, Jaguar Land Rover, Coventry CV3 4LF, United Kingdom

⁴The Dept of Engineering Science, University of Oxford, Oxford OX1 3PJ, United Kingdom

Lithium-ion (Li-ion) batteries have undergone a multitude of improvements and achieved a high level of technological maturity. To further optimise cell performance, an understanding of the failure mechanisms is important. Forty-eight state-of-the-art cylindrical cells in the 21700 format, suitable for electric vehicles, are studied at the beginning-of-life (BOL) and end-of-life (EOL) by X-ray computed tomography (X-ray CT) and image analysis. The results indicate that shifting current collecting tabs closer to the centre of the cell and including a mandrel is likely to suppress the propagation of capacity depleting deformations. It is recommended that manufacturers also try to improve cell assembly processes to form a more uniformly circular jelly roll and use tapered electrodes to minimise the nucleation of deformations.

© 2023 The Author(s). Published on behalf of The Electrochemical Society by IOP Publishing Limited. This is an open access article distributed under the terms of the Creative Commons Attribution 4.0 License (CC BY, <http://creativecommons.org/licenses/by/4.0/>), which permits unrestricted reuse of the work in any medium, provided the original work is properly cited. [DOI: 10.1149/1945-7111/acf883]



Manuscript submitted May 19, 2023; revised manuscript received August 18, 2023. Published September 25, 2023.

In the face of current environmental challenges, the proliferation of electric vehicles is essential to drive changes towards Net Zero. The state-of-health (SOH) of a battery determines its usability in electric vehicles. In the automotive industry, once a cell reaches 80% of its initial capacity, it is generally considered to be at its end-of-life (EOL).^{1,2} Therefore, maximising the output of a cell before it reaches EOL is critical in driving down associated costs and improving performance of electric vehicles. However, the driving forces behind battery performance loss, hence cell degradation, need to be better understood. Gaining an understanding of the factors that drive cells towards EOL in lithium-ion (Li-ion) is therefore critically important.

The conditions in which the batteries are utilised can accelerate degradation by inducing chemical changes within the cells. Batteries for automotive applications are expected to be able to operate in a wide temperature range. However, low temperatures (below 0 °C) can contribute to lithium plating on the negative electrode³ and reduction of electrolyte by the lithium causing a decrease in ionic conductivity.⁴ On the other hand, cycling at elevated temperatures (above 25 °C) leads to an increase in the growth of the solid-electrolyte interphase (SEI) layer,⁵ leading to an increase in the resistance of the cells.⁶ Reduction in capacity is also caused by the irreversible charge consumption⁷ from the increasing growth in SEI. These effects also pose a safety risk as lithium plating can lead to internal shorts, resulting in thermal runaway.

Mechanical degradation occurs in numerous forms, and can also lead to deterioration of capacity. During cycling, the intercalation and de-intercalation of Li⁺ ions can cause volume changes of up to 10% in graphite⁸ and 280% in silicon⁹ anodes. Li-ion cathodes also experience volume changes of up to 5% by Li[Ni_{1-a-b}Co_aAl_b]O₂ (0.05 < x < 0.15 & 0.02 < b < 0.10) (NCA)⁹ and ca. 2% by LiNi_{0.8}Mn_{0.1}Co_{0.1}O₂ (NMC).^{10,11} The stresses associated with this volume expansion can cause electrode cracking and particle fracture. Markervich et al.¹² utilised SEM combined with Raman spectroscopy to demonstrate the damage to graphite crystals due to mechanical stresses from lithium insertion at the micro- and nano-scale, and Taiwo et al.¹³ exhibited bulk silicon particle cracking and the formation of voids in the electrode due to material displacement using X-ray computed tomography (X-ray CT). Liu et al.¹⁴ identified cracking in NCA granules using X-ray CT and determined that this

caused the observed long term capacity loss, they also observed that the electrodes with the best lifetime displayed less cracking. Particle cracking leads to loss of capacity through various mechanisms. Cracked particles expose more active material surfaces to the electrolyte, leading to formation of inorganic materials on those surfaces, increasing resistance, and consuming lithium in the formation of the passivating layer. The formation of SEI can also lead to isolation of the cracked active material as the layer forms around the displaced particles. Additionally, the number of sites suitable for reversible lithium ion accommodation may decrease due to the cracking and formation of new planes which might not be accessible to the electrolyte.¹²

Ageing through electrochemical cycling can also lead to large scale mechanical deformation of the jelly roll, which is attributed to increased capacity fade and accelerated descent towards EOL. Zhao et al.¹⁵ suggest that plastic deformation of particles caused by charge/discharge lead to irreversible change in the shape of the electrodes, while Willenberg et al.¹⁶ attribute jelly roll deformation to the increase in pressure caused by the expansion of the anode. Willenberg et al.¹⁶ also partially associate the deformation to an increase in the diameter of the cylindrical Li-ion cell they observed. Bach et al.¹⁷ and Waldmann et al.¹⁸ ascribe deformations of the jelly rolls to the structure of the cell, such as the “bulk” caused around the current collecting tabs. Waldmann et al.¹⁸ also found that the deformations are more pronounced at higher cycling rates and initiate near the current collecting tabs, which they have partially assigned to the Ohmic heating effects at the tabs. Furthermore, they noticed cells with mandrels, or centre pins, did not show any deformation as they may suppress the deformations. In support of the findings by Waldmann,¹⁸ Kim et al.¹⁹ found through their simulations that the stress experienced by the separator at the Ni-current collecting tab/separator interface was greater than the yield strength of the jelly roll, demonstrating that it's more likely for deformations to occur in line with the tabs.

The exact cause of jelly roll deformation is not yet understood. It may be that stress induced bulk cracking of electrode particles, as discussed above, may compromise the structural integrity of the electrode rolls in a cell, leading to large-scale deformation of the jelly roll, or just the bulk expansion and contraction of the electrodes during cycling may be causing gradual irreversible change in their shape. Similarly, the exact consequence of the deformation is also not well understood, however cell level jelly roll deformation is likely to cause delamination of the active material, resulting in

^zE-mail: paul.shearing@eng.ox.ac.uk

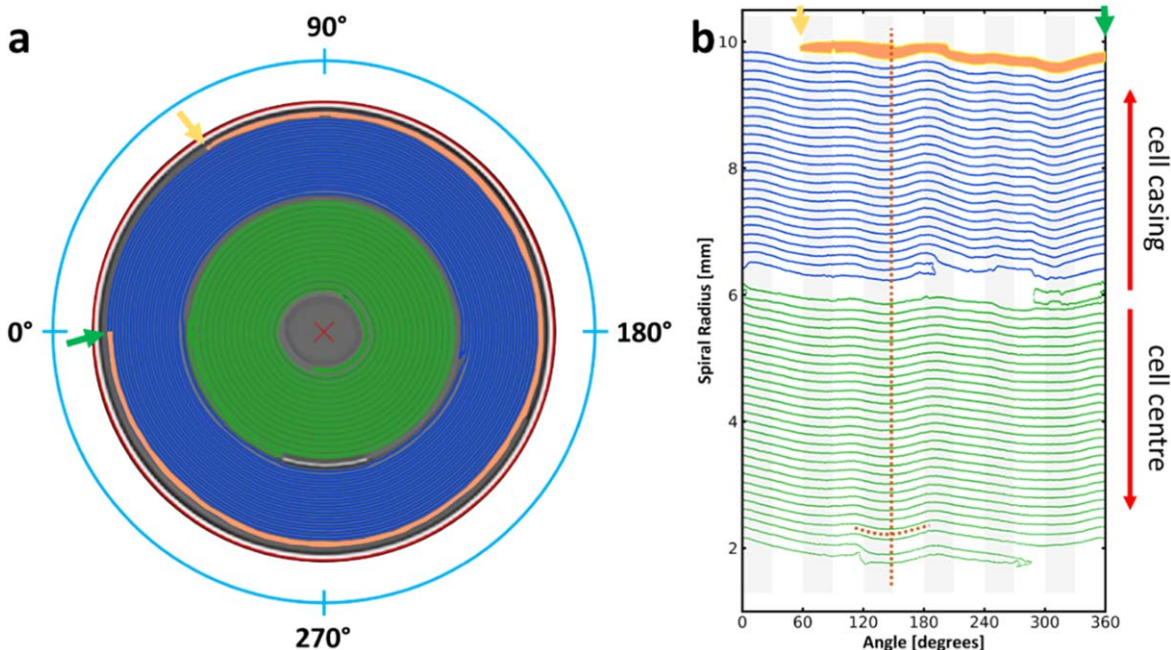


Figure 1. Illustration of the generation of a “virtual unrolling” plot from an X-ray CT slice of one of the cells. The repeating layer (cathode) is highlighted in blue and green as its been split into two sections by the tab in the middle. The red “X” indicates the centre of the cell, and the red circle, the cell casing.

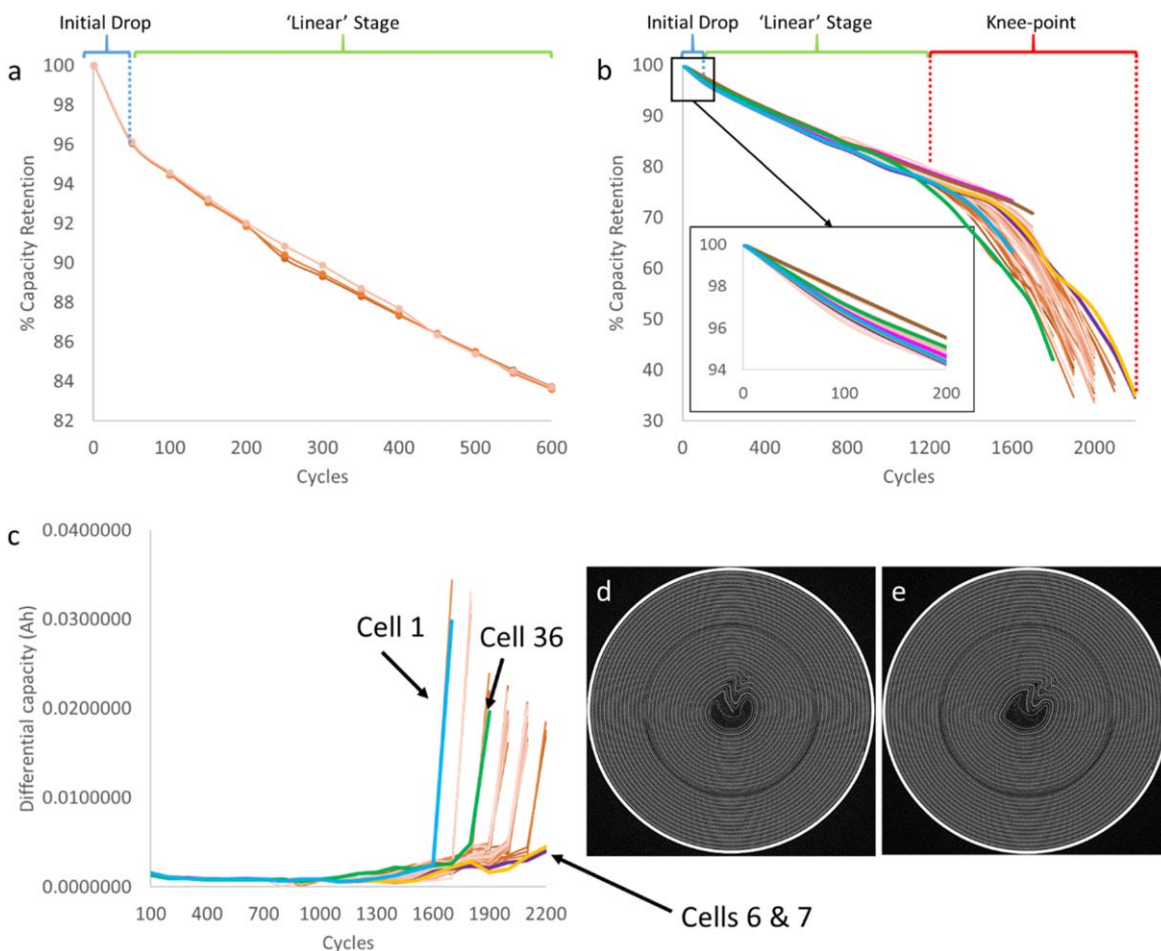


Figure 2. Capacity retention profiles of (a) cells 46–48, (b) cells 01–45, (c) differential capacity profile against the number of cycles showing the point at which cells 01–46 enter the knee-point, and (d)–(e) X-ray CT slices of cycled cells 06 and 07 at point of maximum deformation, respectively. A few data points in (c) have been highlighted for illustration purposes.

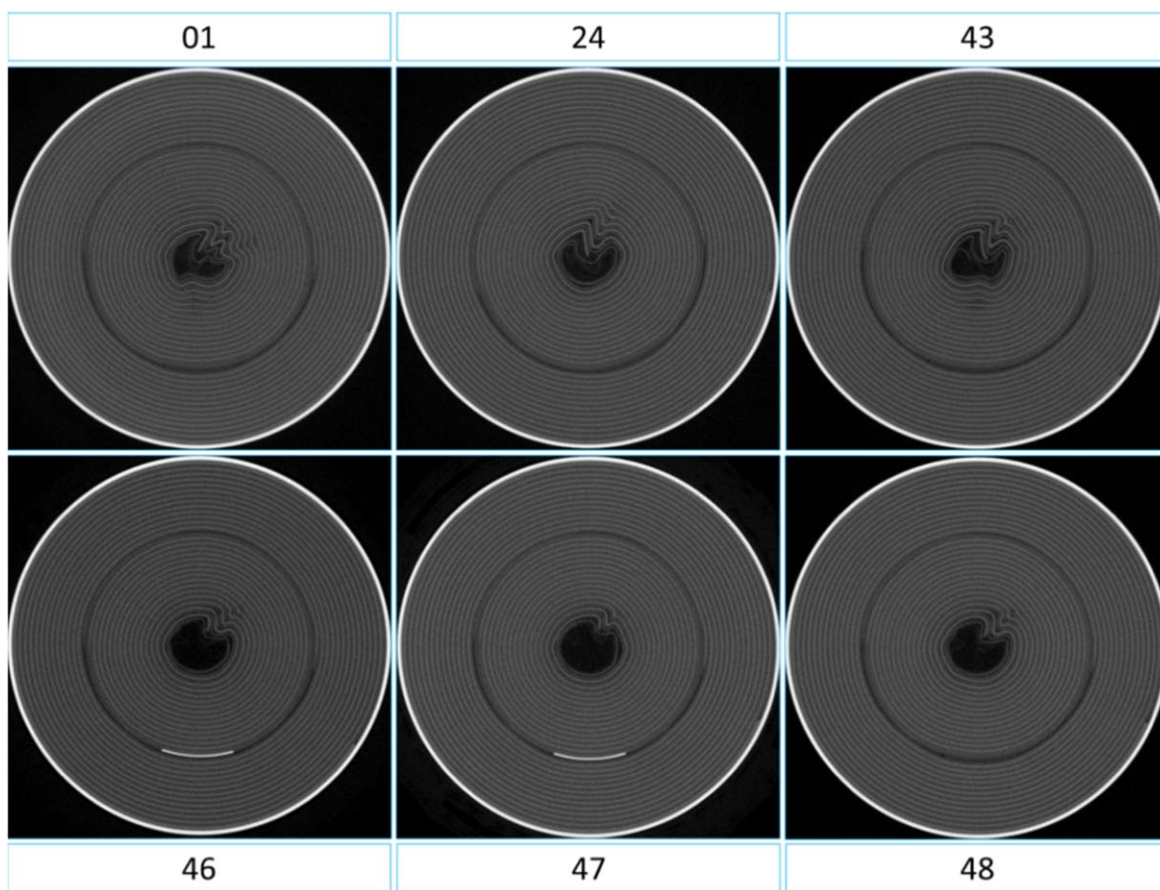


Figure 3. X-ray CT slices of cells 01, 24, 43, after 1600–1700 cycles, and 46, 47, 48 after 600 cycles at point of maximum deformation.

uneven distribution of current and increased resistance. The delamination of the electrodes might also lead to “dead zones” - areas that have lost all contact to the current collector.

“Virtual unrolling” (VU) is an image registration and analysis that resolves the spirally wound electrode rolls in cylindrical cells without the need for disassembly.²⁰ It utilizes the fast, non-destructive image acquisition capabilities of X-ray CT and works, provably,²⁰ even with acquisition periods of less than two minutes. Kok et al.²⁰ first used the technique to correlate cell failure and ageing to the formation of jelly roll deformations nucleating at initial electrode defect sites. Cell quality assurance methods rely heavily on optical detectors²¹ for checking the quality of electrodes before cell assembly, however, that does not take into account any influences arising from the assembly process. VU has the potential for the implementation of a non-destructive, in-line quality assurance procedure that can be carried out as a final step in the manufacturing process and which does not rely on human input through the fast acquisition and analysis of the jelly rolls of pristine cells. This paper will focus on cell level, macro deformations and aim to provide some insight into the manner in which deformations occur, how they progress, and the impact on the structure of the cell.

Methodology

Cell cycling.—Forty-eight state-of-the-art commercial 21700 lithium cells (Ni-rich cathode, graphite/SiO_x anode) were selected for this study and were split into two batches for cycling: batch A containing 45 cells numbered 01–45, and batch B containing the remaining three cells numbered 46–48. The cells from batch A were cycled between 2.5–4.2 V in an environmental chamber (Espec) set to 33 °C using a constant charge/constant voltage (CC/CV) regime with 10 min rest after both charge and discharge. The cells were cycled at 1C for both charge and discharge using Maccor (4000H

series with 0–5 V, 100 A channels), and the current was tapered to C/20 during the CV step on charge. Every 100 cycles, these cells were subjected to reference performance tests (RPTs), which were conducted at 25 °C. The cells were charged to 4.2 V at C/3, tapering current to C/20 during the CV step on charge. After a 60 min rest, the cells were discharged to 2.5 V at C/3 and the measured capacities were taken as the reversible cell capacities. After a 60 min rest step, the cells were once again charged to 4.2 V. Additionally, direct current internal resistance (DCIR) investigations were carried out on the 46 cells using a 2C pulse over 30 s at 100, 80, 50 and 20% state-of-charge (SOC) as part of the RPT every 100 cycles.

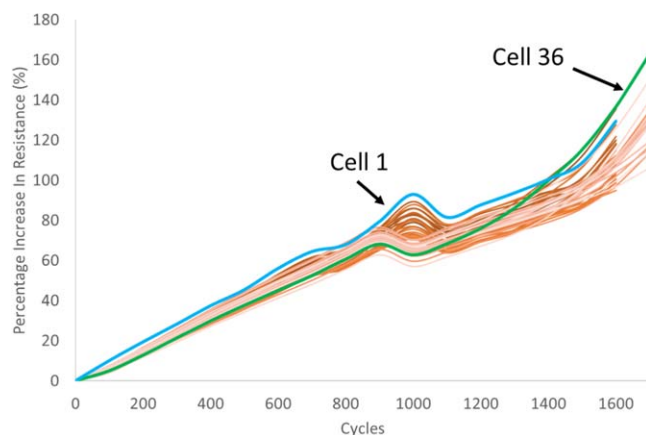


Figure 4. Percentage increase in the resistance of the cells compared to their resistance at the pristine state from the DCIR tests conducted at 100% SOC.

The other three cells (46–48) were cycled using a Maccor battery cycler (Model 4200, Maccor Inc., Tulsa, USA) in an environmental chamber (Maccor Temperature Chamber MTC-020, Maccor Inc.) set to 40 °C. Similarly, these cells were also cycled at 1C charge and discharge using a CC/CV regime between 2.5–4.2 V.

Specific cells have been chosen for discussion and to illustrate important points. Given the number of cells studied here, it is not possible to distinguish every cell with different colours or to add a legend. Thus, the specific cells chosen for discussion have been highlighted in their own specific colours throughout this work for distinction: cell one is cyan; cell 6 is purple; cell 7 is bright orange; cell 24 is pink; cell 36 is green; cell 43 is brown.

X-ray computed tomography.—All the cells were scanned using a Nikon X-ray machine (XT H 225, Nikon Metrology, Tring, UK) at the beginning of their life (pre-cycling) and after all the cycling had concluded. The scans were carried out using an exposure time of 0.5 s, beam energy and current of 200 kV and 210 μ A, respectively. Approximately 1450 projections were taken for each cell. The image reconstruction of the acquired projections was carried out using a filtered back projection algorithm (CT Pro 3D, Nikon Metrology) resulting in a voxel size of 39 μ m.

Additionally, in situ scans were carried out on cells 46–48 every 200 electrochemical cycles. The scans were carried out at six different voltage points during the charge cycle: 2.5, 3.4, 3.6, 3.8, 4.0, and 4.2 V. The charging was carried out at 0.7C, tapering the current to 100 mA at each voltage step, with a step limit of 45 min for the CV process. The scans were truncated, resulting in a voxel size of 12 μ m, using an exposure time of 0.5 s and beam parameters of 195 kV and 210 μ A.

Virtual unrolling.—The digital disassembly process in the “virtual unrolling” of a cell allows for the non-destructive examination of the electrode roll for comparisons between different cells or the same cell at different stages in its life cycle using X-ray CT imaging data. The virtual unrolling process has four principal steps: Firstly, the pre-processing of the X-ray CT data: the pixel intensity of the images are normalised to range from 0 to 1. Secondly, the identification of the centre of the cell: the cell casing is determined by obtaining the longest contour within a certain greyscale threshold, and then the centre is identified by algorithmically trying out all possibilities for the centre within the cell casing that results in the least casing deformation. Thirdly, identifying the electrode roll: the boundary between the anode and cathode is increased by applying small kernel median filters and unsharp masks and this boundary

found in Cartesian coordinates using a modified marching cubes algorithm. Finally these coordinates are translated into cylindrical coordinates as below:

$$r = \sqrt{(x - x_0)^2 + (y - y_0)^2} \quad [1]$$

$$\phi = \arctan\left(\frac{y - y_0}{x - x_0}\right) \quad [2]$$

where, the x,y co-ordinates of the centre of the cell are x_0 and y_0 , respectively.

The distance between these contours is a measure of the thickness of the anode and similarly the change in position in these contours is a measure of strain within the jelly-roll. A single anode “layer” is taken to be a 360° strip of anode material and the thickness measurements were taken from averaging ca. 200 X-ray CT slices from towards the middle of the cells, near the tip of the negative current collecting tab is located. Throughout this work where thickness and strain refer to the distance between these contours and the change in these contours respectively.

Interpretation.—Virtual unrolling translates each 360° rotation of the cathode spiral into a separate layer in the unrolling plot. Figure 1 illustrates the generation of an unrolling plot from a slice of one of the forty-eight cells. The electrode roll has been split into two sections (coloured green and blue) due to the presence of the current collecting tab at the middle of the jelly roll. For illustration purposes, the first cathode layer next to the cell casing is highlighted in orange and the start is denoted by the yellow arrow, and the end of the 360° layer is indicated by the green arrow in Fig. 1a. The translation of that same layer into an unrolled orientation can be seen in Fig. 1b. It can also be seen that this cell contains a pre-existing inflection point in the jelly roll, which is a non-uniform defect due to manufacturing and assembly processes, as highlighted by the vertical dotted orange line in Fig. 1b. This inflection point is present throughout the whole jelly roll along the same angle, as highlighted by the dotted orange line.

Results and Discussion

The forty-five cells from batch A were cycled until the knee point was visible for the majority of the cells and the three cells from batch B were cycled for 600 cycles. The capacity retention for all the cells can be seen in Fig. 2. After 600 cycles, the cells from batch A have a

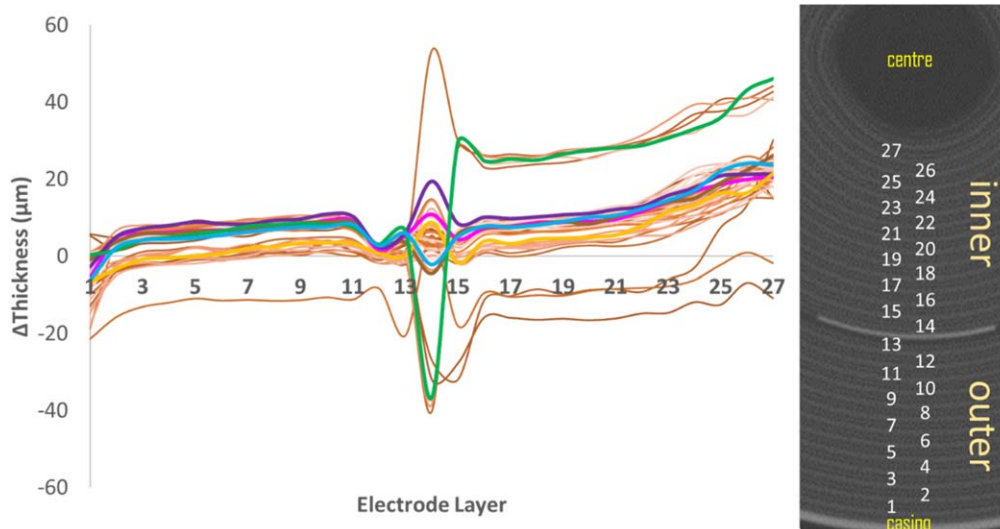


Figure 5. Anode thickness change for the cells in batch A. The x-axis indicates the anode layer corresponding to the labelled X-ray CT slice. The calculations were carried out towards the middle of the cells, at the tip of the negative tab.

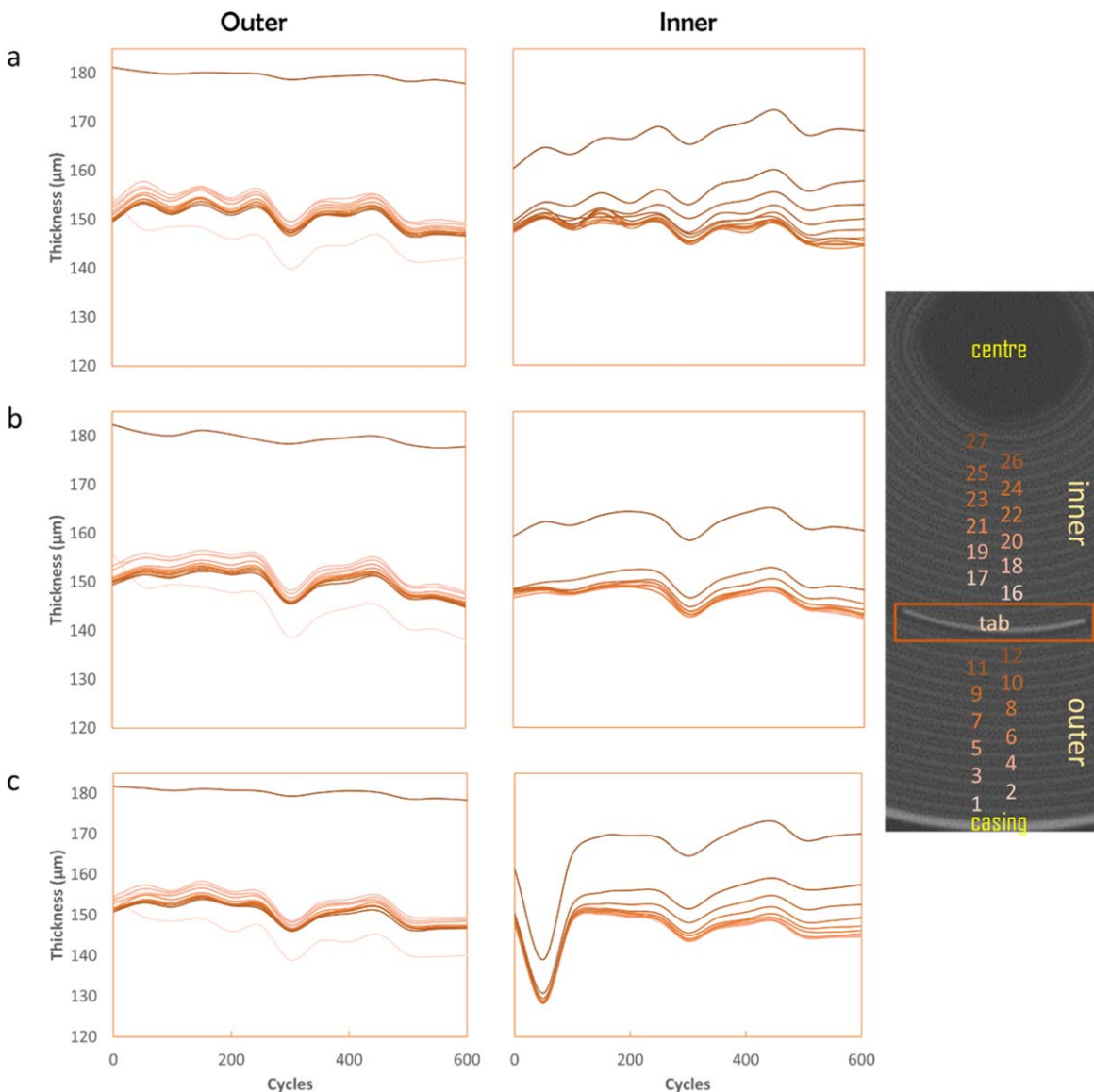


Figure 6. Anode thickness change for the cells in batch B (a) Cell-46, (b) Cell-47, and (c) Cell-48, respectively. The x-axes indicate the anode layer corresponding to the labelled X-ray CT slice. The plots have been split into two: the inner section (after the tab), where the darker lines represent the layers closer to the cell centre, and the outer section (before the tab), where the darker lines represent layers closer to the cell tab. The calculations were carried out towards the middle of the cells, at the tip of the negative tab.

capacity retention within the 85%–90% range, however, the cells from batch B are below 84%. The greater degradation could be the impact of cycling at a slightly elevated temperature of 40 °C compared to 33 °C, leading to greater solid electrolyte interphase (SEI) build-up at the surface of the electrodes and a greater rate of active material loss. Cells from both batches show the typical accelerated capacity fade in the initial stages of cycling²² as highlighted by the blue lines in Figs. 2a & 2b, associated with the evolution of the interface layers at the surface of the cathode and anode. Then, a quasi-linear stage of capacity fade is observed. A capacity “knee-point” is a secondary accelerated drop in capacity retention observed in cells undergoing long term electrochemical cycling. From Fig. 2b, it can be seen that the cells in batch A reach a knee-point in capacity fade at different points in their cycling, as highlighted by the red dotted lines. Six hundred cycles was not sufficient to reach the knee-point for any of the cells in batch B. The point at which the cells in batch A experience the most capacity fade can be more clearly observed when looking the differential capacity plotted vs the number of cycles in Fig. 2c. Although the differential capacity starts to increase before 1500 cycles, there is a sharp

increase in the last 100 cycles of the cells’ cycling period for most cells, which is the knee-point. After 1600 cycles, there are only two cells in batch A which do not experience the same rate of capacity fade as the other cells—cells 06 and 07—and their X-ray slices after cycling can be seen in Figs. 2d & 2e. Additionally, X-ray CT slices of the three cells with the earliest knee-point (cells 01, 24, and 43) can be seen in Fig. 3. Compared to cells 06 and 07 which did not exhibit a knee-point, those cells show a more severe deformation of the jelly roll, and in some cases, multiple deformations can be observed. Figure 3 also contains X-ray CT slices for the cells in batch B after 600 cycles. It can be seen that the nucleation of deformation has occurred in the cells in batch B, but they have not progressed to the level show in batch A due to the lower number of electrochemical cycles performed. It is clear that greater electrochemical cycling leads to the formation of more severe and numerous deformations in the jelly rolls of cylindrical cells, and it is also clear that as at some point the deformations reach a “break-point” that causes a secondary, rapid decrease in capacity.

Figure 4 shows the results of the DCIR tests carried out on the cells at 100% SOC. It shows the percentage increase in the resistance

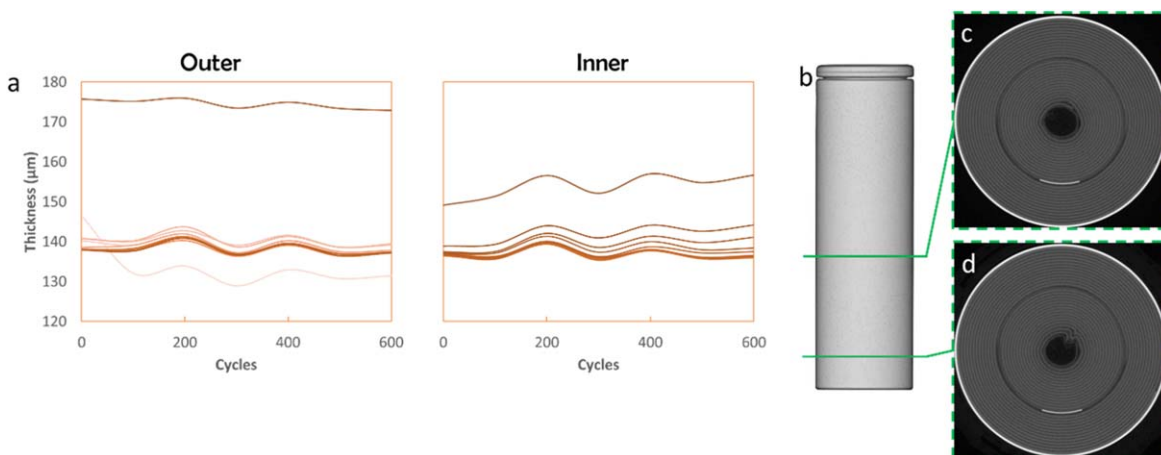


Figure 7. (a) anode thickness change for Cell-47 at a point of deformation, (b) a 3D render of Cell-47, (c) a slice at a point where there is no deformation, and (d) a slice at a point of deformation. The plots in (a) have been split into two: the inner section (after the tab), where the darker lines represent the layers closer to the cell centre, and the outer section (before the tab), where the darker lines represent layers closer to the cell tab.

at all points up to 1700 cycles compared to the initial resistance values at the pristine state. It can be seen that the spread of the increase in resistances starts to widen as the cells are cycled. Even if the cells are from the same manufacturing batch, there are small variances in active material loading and electrode arrangement causing these differences. Cell 1 consistently has the highest increase in resistance for most of the cycling period. In return, it has one of the earliest knee-point (1600 cycles) as seen in Fig. 2. Additionally, cell 36 overtakes cell 1 to have the highest rate of increase after 1400 cycles, and also has one of the earliest knee-points in batch A, suggesting that the cells with a greater rate of increase in DCIR are indicative of greater capacity fade. DCIR measures the Ohmic resistance resulting from the electrodes, current collectors, electrical connections, and the conductivity of the electrolyte. The connection between DCIR and the knee-point could be described by the loss in active material and the loss of contact with the current collectors due to the propagation of deformations within the jelly rolls of the cells. A feature of interest in the DCIR result is the dip in the rate of resistance increase at 1000 and 1100 cycles, which seems to split the cells into two clusters. The cause for this is unclear, however, all the cells in both clusters follow the same trend, and both clusters re-join to exhibit a uniform trend, so it is assumed to be an artefact caused by the experimental set-up.

The change in anode thickness over the whole cycling period for batch A can be seen in Fig. 5, where the x -axis corresponds to the numbered anode layers in the X-ray CT slice. The anode comprises of a mixture of graphite and silicon (SiO_x), and as such the expectation would be an irreversible increase in thickness over time. However, it can be seen that for the first layer (outer) there is actually a net *decrease* in thickness, which can be assigned to the fact that the strain from the expansion of the electrodes is directed towards the cell casing,²³ thus the layers closest to the casing would be compressed between the casing and the expanding inner layers. Furthermore, Kim et al.¹⁹ found through their finite element model that the greatest stress was experienced by the separator next to the current collecting tab, which was located between the tab and the cell casing. In our case, the tab is located in the middle of the casing and the cell centre, thus by extrapolation, the greatest stress might be experienced by the layers between the tab and the casing, resulting in some of the compression of the layers. All the layers experience some form of thickness change, but, the biggest increase is experienced by the centremost layers, exhibiting that the irreversible change occurs from the inside out. The current collecting tab is located between the anode layers 13 & 14, and when examining Fig. 5, it would appear that the tab is suppressing some of the expansion propagating throughout the layers. The irreversible expansion of the electrodes leads to increased strain on the jelly

roll, and results in electrode deformation and then delamination of the active material from the current collecting foil, leading to capacity loss. Therefore, it may be of benefit to move the current collecting tab more towards the centre of the cell to suppress the volume expansion in more layers. It has been noted that the inclusion of a mandrel also suppresses the deformation of the electrodes at the centre of the cell,¹⁸ so a combination of a mandrel and a shift of the tabs closer to the centre might lead to less deformations and longer cell life. However, this may inadvertently lead to suppression of the stress related to electrode expansion in both directions radially and cause a burst of pressure at some point. Whilst the re-design of cell architectures is outside of the remit of this paper, it illustrates the possibility of using this technique to inform cell design strategies.

Cells 46–48 were scanned every 50 cycles, which allows for the examination of the internal changes in the jelly roll at a more granular temporal resolution, as shown in Fig. 6. The change in thickness of the anode layers is split into two clusters, before the tab, and after. From these higher temporal resolution scans, it is clear that there is definitely a divide between the electrode layers before and after the tab (the inner and outer sections illustrated in Fig. 4): the anode layers before the tab and closer to the cell casing experience compression over time, whereas the layers after the tab experience expansion, starting with the innermost layers. Furthermore, there is a wave-like pattern to the compression and expansion, which is likely due to the degree of reversibility of the electrode expansion caused by the Li^+ ion intercalation/alloying. Analysis into whether deformations cause greater thickness changes were carried out on cell 47. For consistency, all the thickness change analysis presented thus far were carried out at the same point for all cells, relative to their current collecting tab, and as such the result for cell 47 in Fig. 6b shows the change in thickness of the anode layers at a point where there is no deformation. Complementary data in Fig. 7a shows the thickness changes for 47 at a point where there is deformation. When comparing the two figures, it can be seen that in the absence of a deformation, the initial thickness of the anode is greater (ca. $150\ \mu\text{m}$) than at the point of deformation (ca. $140\ \mu\text{m}$). However, when comparing the layers, for example layer 27, at the point of no deformation there is little change between the initial and final anode thicknesses, whilst at the point of deformation there is an increase from ca. $150\ \mu\text{m}$ to $157\ \mu\text{m}$. The difference in the initial anode thicknesses at the different points in the cell demonstrates the variance caused by standard manufacturing and assembly processes. A 3D rendering of the cell and slices at a point of deformation and at a point where there is no deformation are shown in Figs. 7b–7d for reference. Non-uniform current distribution leads to uneven utilisation of active materials and gradients in temperature and potential.^{24,25} This becomes increasingly severe as the discharge progresses, and the effect is stronger closer to the negative current

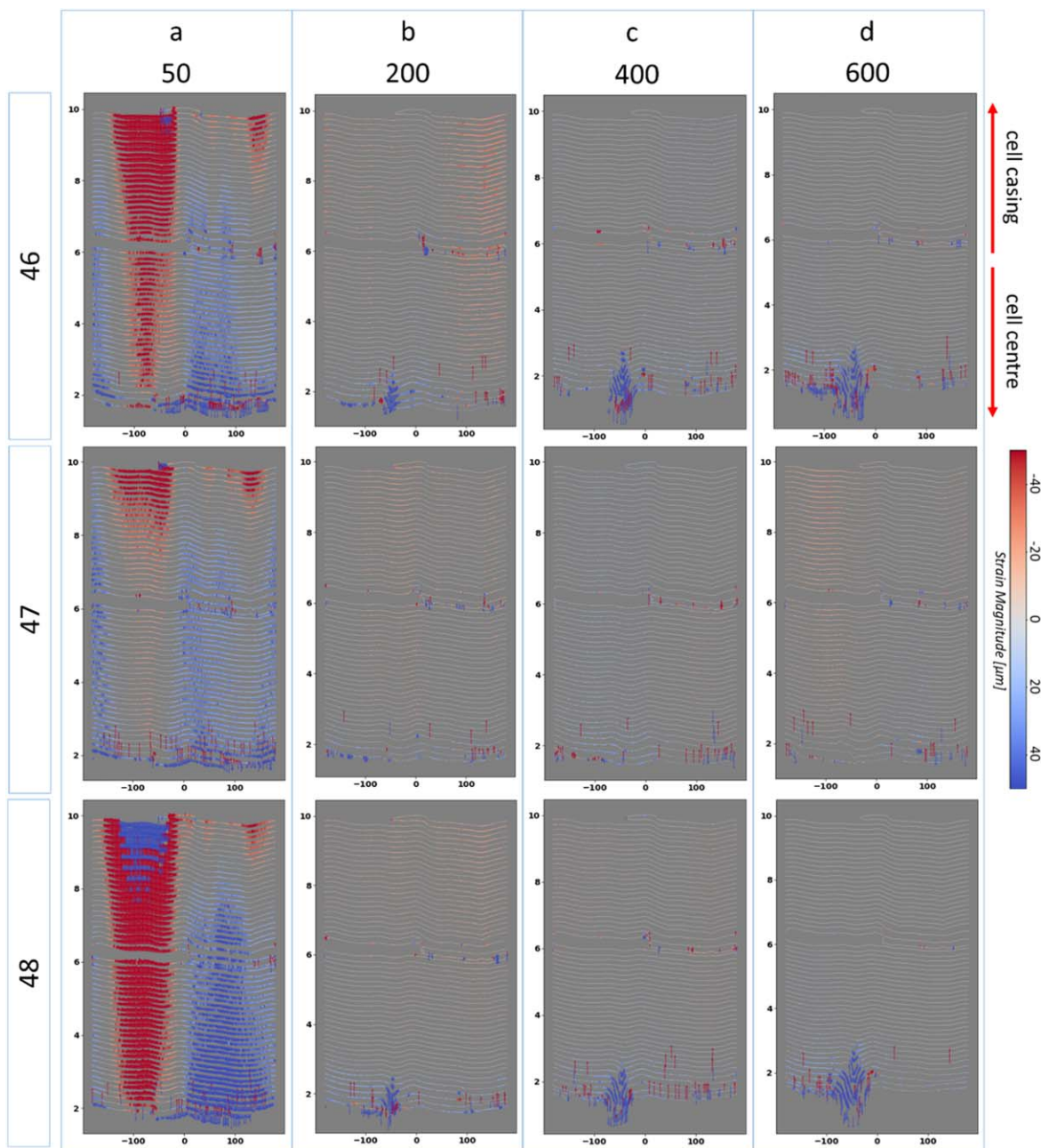


Figure 8. Strain distributions for cells 46–48 (a) pristine to 50 cycles, (b) 150 cycles to 200 cycles, (c) 350 cycles to 400 cycles, and (d) 550 cycles to 600 cycles. The deeper red indicates greater compression, and the deeper blue a greater expansion. The calculations were carried out towards the middle of the cells, at the tip of the negative tab.

collecting tab.²⁶ It has been previously demonstrated by Zhang et al.²⁷ that a cell configuration with one positive tab produces a more non-uniform current distribution leading to poor performance. The cells contain one of each positive and negative current collecting tabs, therefore it is expected to have highly uneven current and temperature distributions throughout the electrodes. As such, there will be non-uniform active material utilisation and electrochemical activity throughout the jelly roll, which results in sections of the anode experiencing more Li^+ intercalation/alloying and resultantly more drastic expansion and contraction during electrochemical cycles ultimately leading to electrode collapse and deformations. This explains the increased anode thickness changes observed at the deformations and also explains the greater number of deformations observed on the bottom half of the cells in batch A (as shown in Fig. A3 in the supplementary information (SI)) where the negative current

collecting tab is present. For reference, the X-ray slices of all 48 cells in their pristine state can be found in Figs. A1 and A2 in the SI.

Figure 8 shows the strain distributions in the jelly rolls of cells 46–48 as a function of cycling. The strains show that across the cell there is a re-arrangement of the jelly roll during initial cycling—the period when the initial accelerated drop in capacity is observed. This indicates that a larger change in the jelly roll has a greater impact on the degradation of capacity. For reference, for cell 46 the decrease in discharge capacity between the first and 50th cycle was 3%, whereas between 50th to 200 cycles it was 4%. For cells 47 and 48 both it was 2% and 4%, respectively. The red sections indicate a compression of the electrodes towards the cell casing, and the blue indicates an expansion towards the cell centre. It can be seen that during the initial re-arrangement, the electrode fills out the space between the cell casing and the jelly roll. Where there is no space on the outside,

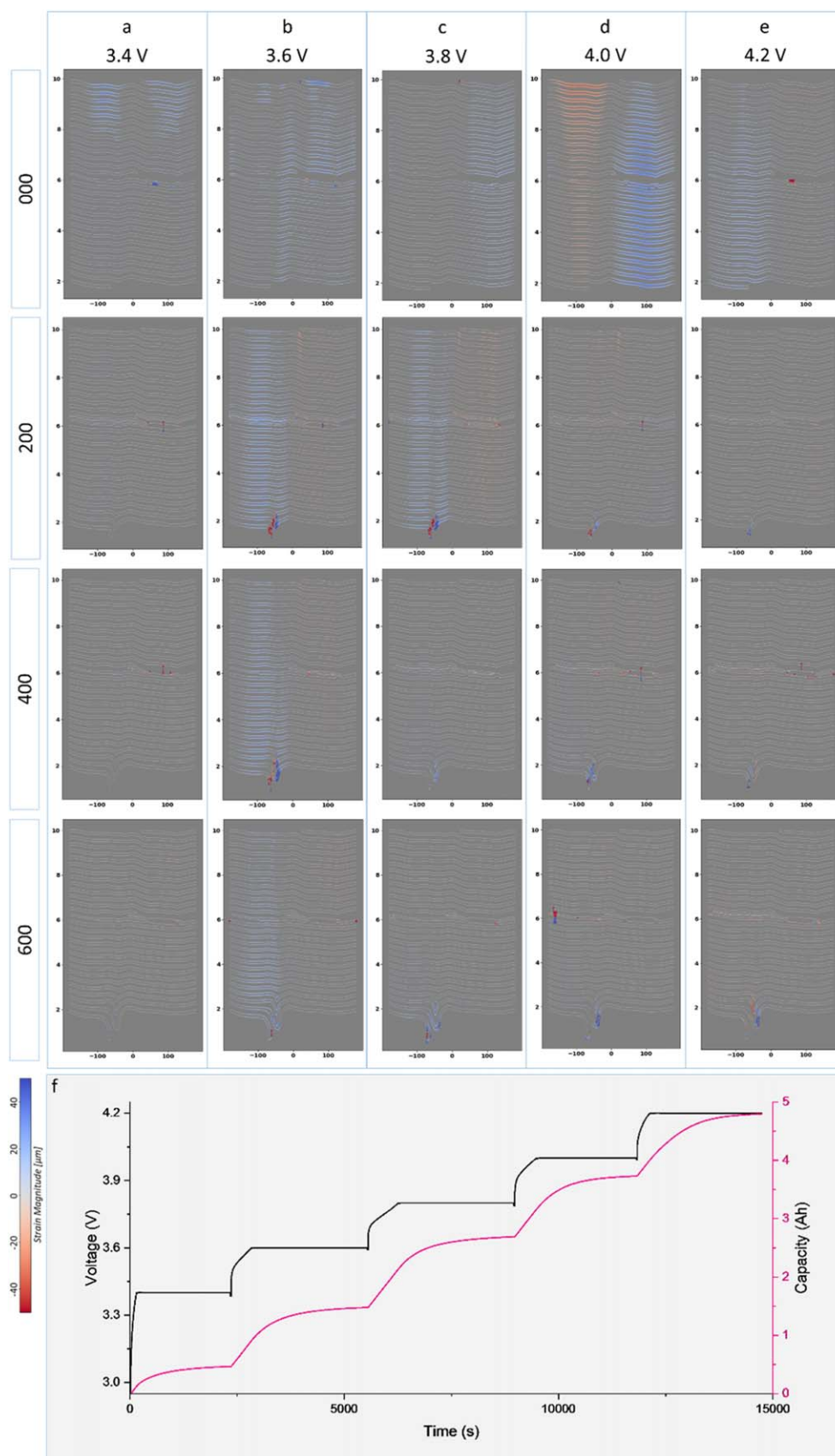


Figure 9. Strain distributions for Cell-48 (a) 2.5 V to 3.4 V, (b) 3.4 V to 3.6 V, (c) 3.6 V to 3.8 V, (d) 3.8 V to 4.0 V, and (e) 4.0 V to 4.2 V. The voltage profile at the pristine state (000) is shown in (f). The deeper red indicates greater compression, and the deeper blue a greater expansion. The calculations were carried out towards the middle of the cells, at the tip of the negative tab.

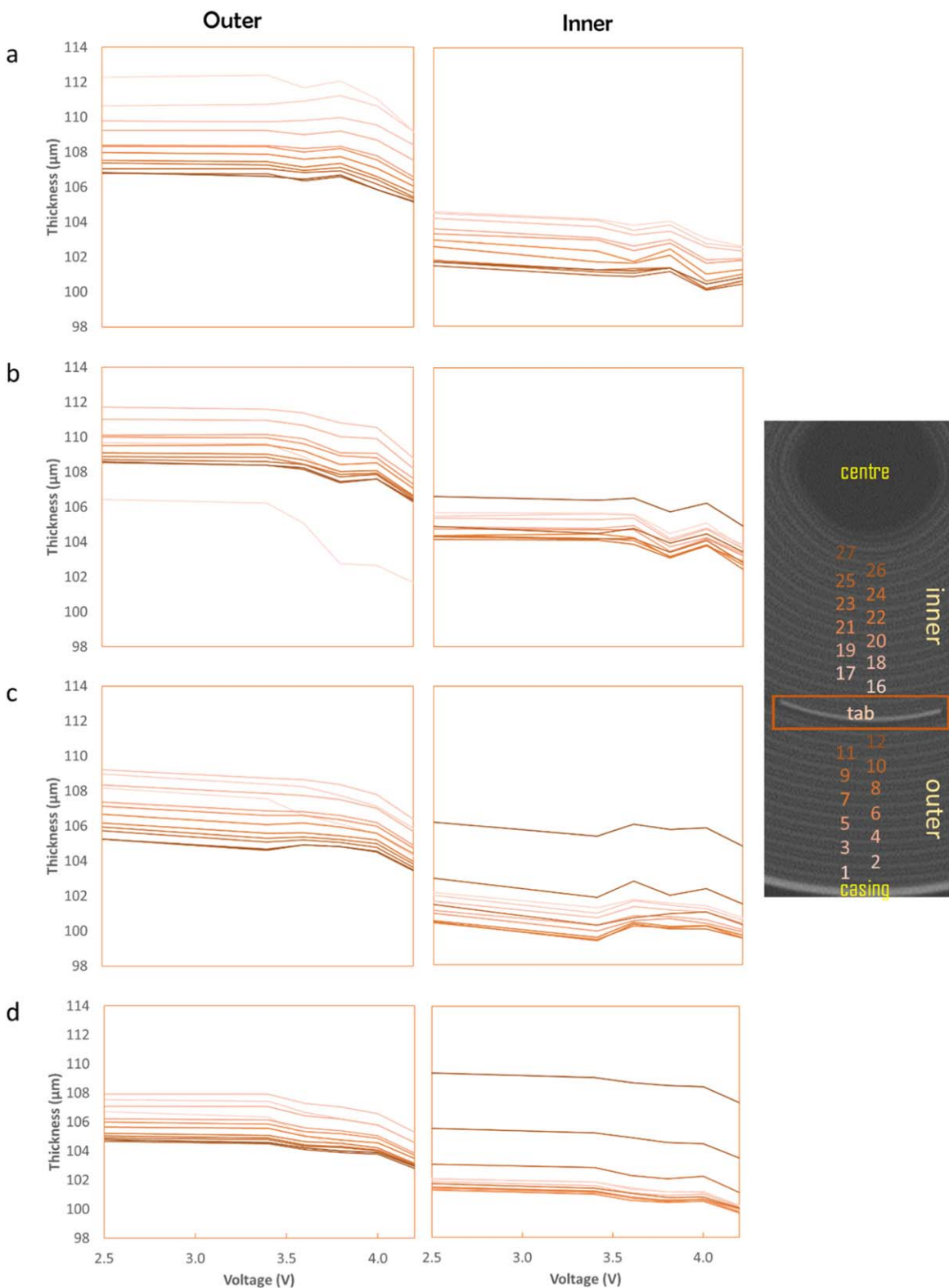


Figure 10. Anode thickness change for the Cell-48 at different voltage points (a) pristine, (b) 200 cycles, (c) 400 cycles, and (d) 600 cycles, respectively. The x-axes indicate the anode layer corresponding to the labelled X-ray CT slice. The plots have been split into two: the inner section (after the tab), where the darker lines represent the layers closer to the cell centre, and the outer section (before the tab), where the darker lines represent layers closer to the cell tab. The calculations were carried out towards the middle of the cells, at the tip of the negative tab.

the jelly roll is forced to expand towards the centre of the cell—the only other available space. In the later cycles, the strain from the expansion and contraction of the electrodes becomes focused on the inflection points in the spiral, defined as the pre-existing non-circular

(non-linear in the strain distribution plots) arrangement of the electrode roll due to manufacturing and assembly processes. The deformations nucleate at the inflection points and continue to expand and proliferate throughout the layers, from the centre layers to the

outer layers towards the direction of the cell casing, similar to the observations with the anode thickness changes, further evidence that the swelling of the electrodes leads to the deformation.

To investigate the effects of (de)lithiation on the mechanical changes in the jelly roll, cells 46–48 were subjected to in situ scans at six different voltage steps at the beginning of life and every 200 cycles thereafter. The cells were scanned in their discharged state, and the cell was charged while mounted on the X-ray machine stage and scanned at 3.4 V and then every 200 mV thereafter up to 4.2 V. Figure 9 shows the strain distributions for cell 48 at the different voltage steps throughout its cycling period. It can be seen that the biggest rearrangement of the jelly roll occurs at the beginning of life, and afterwards the most change occurs between 3.6 V and 4.0 V, primarily at 3.6 V. A point of note is that the jelly roll deformation appears to be nucleating between the two opposing forces of outwards compression and inwards expansion. This is illustrated by comparing the strain distributions at 4.0 V at the beginning of life (Fig. 9d at 000 cycles) and at the location of the deformation that appears after cycling in (Fig. 9b at 200 cycles). Figure 10 shows the resulting anode thickness change for cell 48. For the outer layers, initially there is a large spread of thicknesses ca. 106–112 μm , and after 600 cycles, not only does the thickness of the anode layers decrease, the spread also decreases: ca. 104–108 μm . This change is consistent over the whole voltage range. It can also be seen that there is little change in anode thickness until the voltage reaches 3.6 V, similar to the strain distribution. As for the inner layers, the thicknesses of the anode layers have a relatively low spread, however, with cycling, the inner most layer starts to increase in thickness. Once the innermost layer reaches a thickness of ca. 106 μm , the layer before it starts to increase in thickness as well, and thus the spread in layer thicknesses starts to widen. The anode layers closer to the middle start to become thinner and the spread in thicknesses shrinks, possibly due to the crushing effect of the expansion in the inner layers. Similarly to the outer section, these changes are consistent over the whole voltage range.

From the voltage profile, it can be seen that from 3.6 V every 0.2 V increase leads to ca. 20% capacity increase, and the biggest increase in capacity occurs between 3.6–3.8 V which might be the cause of the greater shift between 3.6 V and 3.8 V. Also of interest is that the anode seems to contract slightly between 4.0 and 4.2 V, however, over the full course of the cycling period, the inner anode layers increase in size. The same trend is shown by the other two cells in batch B, as seen in Figs. A4–A5 in the SI. Thus, over a single charge cycle, the electrochemical processes cause changes in the thicknesses of the electrodes, causing expansion and contraction forces to spread throughout the electrode layers, and also eventually lead to the irreversible increase in the thicknesses of the anodes. Through the combination of these two effects, over the lifetime of a cell, jelly deformations nucleate at regions where the expansion and contraction forces collide and where the structural integrity of the jelly roll is compromised due to the expansion of the anode.

From the vast number of 21700 cells studied in this work, it has become clear that increased electrochemical cycling leads to jelly roll deformation and that DCIR may be a potential tool to differentiate the cells that are more likely to fail from the less likely to fail cells. It's also likely that the current collecting tabs suppress some of the forces causing deformation, thus it may be prudent to add additional tabs and move them closer to the centre of the cell. The increase in electrode thickness starts at the centre of the cell and propagates towards the outer layers, and data points towards the negative current collecting tab having a bigger influence on the nucleation of deformations, possibly due to uneven current distributions, thus another case for increasing the number of tabs.

Conclusions and Future Work

Forty-eight commercial cells for electric vehicles were tested to gain an understanding behind the mechanisms of cell capacity fade and degradation. It was found that deformation of the jelly roll leads to a knee-point (or a secondary dip in capacity retention) which arises as a

result of the thickening of the electrode in the cells. It was determined that the current collecting tabs suppress the propagation of the expansion of the electrodes and so it may be of benefit for the automotive industry to shift the tab closer to the centre of the cell and also add a mandrel to suppress deformation and potentially increase the cycle life of the cells. As a counter point, this would lead to a reduction in the cell energy density and may lead to a decrease in the safety rating of the cells as the strains behind the expansion of the electrodes might lead to pressure build-up. Additionally, it may be of benefit to increase the number of tabs in the cell to improve current distribution, as non-uniform current distribution and active material utilisation may be one of the factors causing the deformations; this is a known strategy in high power cells, but may also have lifetime benefits for energy cells.

It was also determined that there is a cell wide re-arrangement of the electrode rolls during the initial cycles, which contributes to the initial drop in capacity retention experienced by most lithium-ion cells. Further cycling then leads to the nucleation of deformations at pre-existing inflection points caused by manufacturing processes. Therefore, improving manufacturing processes to create a more uniform (circular) jelly roll may be the most important factor for improving cell life. One option would be to taper the electrode ends, as non-tapered ends leave spaces between the cell casing and jelly roll for the shift of electrodes to occur, and the deformations appear between the two opposing strains of expansion and contraction.

The virtual unrolling technique demonstrated here would prove useful for the electric vehicle manufacturing industry to detect end-of-line manufacturing defects and could also potentially be useful for cell life predictions. Further work can be carried out in order to improve the technique and understanding of the cell behaviours explored here, for example, carrying out additional investigations into the cells in batch B to determine when and how they reach the knee-point. Additionally, applying this technique to investigate cells with multiple current-collecting tabs, and “tabless” 4680 cells would provide valuable information on the prospective batteries of the future.

Acknowledgments

This work was carried out with funding from the Faraday Institution (faraday.ac.uk; EP/S003053/1), grant number FIRG003, FIRG0025, FIRG0028 and the “Silicon Evolve” project; and the EPSRC grant EP/R020973/1. PRS would like to acknowledge the Royal Academy of Engineering (CIET1718/59) for financial support.

ORCID

Paul R. Shearing  <https://orcid.org/0000-0002-1387-9531>

References

1. S. Saxena, C. Le Floch, J. MacDonald, and S. Moura, “Quantifying EV battery end-of-life through analysis of travel needs with vehicle powertrain models,” *J. Power Sources*, **282**, 265 (2015).
2. M. O. Ramoni and H.-C. Zhang, “End-of-life (EOL) issues and options for electric vehicle batteries,” *Clean Technol. Environ. Policy*, **15**, 881 (2013).
3. J. Fan and S. Tan, “Studies on charging lithium-ion cells at low temperatures,” *J. Electrochem. Soc.*, **153**, A1081 (2006).
4. M. Petzl, M. Kasper, and M. A. Danzer, “Lithium plating in a commercial lithium-ion battery—A low-temperature aging study,” *J. Power Sources*, **275**, 799 (2015).
5. T. Waldmann, M. Wilka, M. Kasper, M. Fleischhammer, and M. Wohlfahrt-Mehrens, “Temperature dependent ageing mechanisms in Lithium-ion batteries - A Post-Mortem study,” *J. Power Sources*, **262**, 129 (2014).
6. J. B. Robinson et al., “Non-uniform temperature distribution in Li-ion batteries during discharge—A combined thermal imaging, X-ray micro-tomography and electrochemical impedance approach,” *J. Power Sources*, **252**, 51 (2014).
7. P. Novák et al., “The complex electrochemistry of graphite electrodes in lithium-ion batteries,” *J. Power Sources*, **97–98**, 39 (2001).
8. Y. Qi, H. Guo, L. G. Hector, and A. Timmons, “Threefold increase in the Young's modulus of graphite negative electrode during lithium intercalation,” *J. Electrochem. Soc.*, **157**, A558 (2010).
9. A. J. Louli, J. Li, S. Trussler, C. R. Fell, and J. R. Dahn, “Volume, pressure and thickness evolution of li-ion pouch cells with silicon-composite negative electrodes,” *J. Electrochem. Soc.*, **164**, A2689 (2017).
10. S. C. Yin, Y. H. Rho, I. Swainson, and L. F. Nazar, “X-ray/neutron diffraction and electrochemical studies of lithium De/Re-intercalation in $\text{Li}_{1-x}\text{Co}_{1/3}\text{Ni}_{1/3}\text{Mn}_{1/3}\text{O}_2$ ($x = 0 \rightarrow 1$),” *Chem. Mater.*, **18**, 1901 (2006).

11. O. Dolotko, A. Senyshyn, M. J. Mühlbauer, K. Nikolowski, and H. Ehrenberg, "Understanding structural changes in NMC Li-ion cells by in situ neutron diffraction." *J. Power Sources*, **255**, 197 (2014).
12. E. Markervich, G. Salitra, M. D. Levi, and D. Aurbach, "Capacity fading of lithiated graphite electrodes studied by a combination of electroanalytical methods, Raman spectroscopy and SEM." *J. Power Sources*, **146**, 146 (2005).
13. O. O. Taiwo et al., "Investigation of cycling-induced microstructural degradation in silicon-based electrodes in lithium-ion batteries using X-ray nanotomography." *Electrochim. Acta*, **253**, 85 (2017).
14. H. Liu et al., "Intergranular cracking as a major cause of long-term capacity fading of layered cathodes." *Nano Lett.*, **17**, 3452 (2017).
15. K. Zhao, M. Pharr, S. Cai, J. J. Vlassak, and Z. Suo, "Large plastic deformation in high-capacity lithium-ion batteries caused by charge and discharge." *J. Am. Ceram. Soc.*, **94**(suppl. 1), s226 (2011).
16. L. K. Willenberg, P. Dechent, G. Fuchs, D. U. Sauer, and E. Figgemeier, "High-precision monitoring of volume change of commercial lithium-ion batteries by using strain gauges." *Sustain.*, **12**, 55 (2020).
17. T. C. Bach et al., "Nonlinear aging of cylindrical lithium-ion cells linked to heterogeneous compression." *J. Energy Storage*, **5**, 212 (2016).
18. T. Waldmann, S. Gorse, T. Samtleben, G. Schneider, V. Knoblauch, and M. Wohlfahrt-Mehrens, "A mechanical aging mechanism in lithium-ion batteries." *J. Electrochem. Soc.*, **161**, A1742 (2014).
19. S. Kim, Y. S. Lee, H. S. Lee, and H. L. Jin, "A study on the behavior of a cylindrical type Li-Ion secondary battery under abnormal conditions." *Materwiss. Werksttech.*, **41**, 378 (2010).
20. M. D. R. Kok et al., "Virtual unrolling of spirally-wound lithium-ion cells for correlative degradation studies and predictive fault detection." *Sustain. Energy Fuels*, **3**, 2972 (2019).
21. J. Kurfer, M. Westermeier, C. Tammer, and G. Reinhart, "Production of large-area lithium-ion cells—Preconditioning, cell stacking and quality assurance." *CIRP Ann.*, **61**, 1 (2012).
22. Z. Wu et al., "Graphene anchored with Co₃O₄ nanoparticles as anode of lithium ion batteries with enhanced reversible capacity and cyclic performance." *ACS Nano*, **4**, 3187 (2010).
23. A. Jnawali, A. N. P. Radhakrishnan, M. D. R. Kok, F. Iacoviello, D. J. L. Brett, and P. R. Shearing, "Motion-enhancement assisted digital image correlation of lithium-ion batteries during lithiation." *J. Power Sources*, **527**, 231150 (2022).
24. A. Samba, N. Omar, H. Gualous, O. Capron, P. Van Den Bossche, and J. Van Mierlo, "Impact of tab location on large format lithium-ion pouch cell based on fully coupled tree-dimensional electrochemical-thermal modeling." *Electrochim. Acta*, **147**, 319 (2014).
25. P. J. Osswald, S. V. Erhard, J. Wilhelm, H. E. Hoster, and A. Jossen, "Simulation and measurement of local potentials of modified commercial cylindrical cells." *J. Electrochem. Soc.*, **162**, A2099 (2015).
26. G. Zhang, C. E. Shaffer, C.-Y. Wang, and C. D. Rahn, "In-situ measurement of current distribution in a li-ion cell." *J. Electrochem. Soc.*, **160**, A610 (2013).
27. G. Zhang, C. E. Shaffer, C.-Y. Wang, and C. D. Rahn, "Effects of non-uniform current distribution on energy density of li-ion cells." *J. Electrochem. Soc.*, **160**, A2299 (2013).